

# Supplementary Information: Gain-Based Computing with Manifold Reduction of Soft-Spins vs Quantum Annealing in Ising Hamiltonian Minimization

James S. Cummins<sup>1</sup>, Hayder Salman<sup>2,3</sup> and Natalia G. Berloff<sup>1,\*</sup>

<sup>1</sup>*Department of Applied Mathematics and Theoretical Physics,  
University of Cambridge, Wilberforce Road, Cambridge CB3 0WA, United Kingdom*

<sup>2</sup>*School of Mathematics, University of East Anglia,  
Norwich Research Park, Norwich, NR4 7TJ, UK,*

<sup>3</sup>*Centre for Photonics and Quantum Science, University of East Anglia,  
Norwich Research Park, Norwich, NR4 7TJ, UK*

## PRINCIPLES OF OPERATION OF GAIN-BASED COMPUTING SYSTEMS, QUANTUM ANNEALING, AND SIMULATED ANNEALING

Gain-based computing is a computational paradigm where problems are encoded in the gain and loss rates of driven-dissipative systems, as illustrated in Fig. (1)(a). These systems undergo a symmetry-breaking transition when various physical modes are excited from the vacuum state. As these modes grow, the loss function evolves until a coherent state that minimizes losses emerges. The mode that achieves the minimum of the loss function is amplified, as shown in Fig. (1)(a). Gain-based computing leverages soft-spin models, which provide enhanced dimensionality and small energy barriers during amplitude bifurcation. Although these models create a complex energy landscape with numerous local minima, making optimization challenging, they are also rich in potential solutions.

Simulated annealing (SA), on the other hand, is a classical optimization technique; see Fig. (1)(b). SA probabilistically explores the solution space by simulating the cooling of a material to reach a state of minimum energy. It uses thermal fluctuations to escape local minima, as the system trajectory shown in blue indicates, with the probability of accepting worse solutions decreasing over time. This simulates a cooling process that gradually refines the search towards the global minimum. Implemented on classical computing systems using stochastic algorithms, SA explores the energy landscape by thermal fluctuations, with a gradual reduction in temperature controlling the balance between exploration and exploitation. The performance of simulated annealing is influenced by the cooling schedule, which determines how the temperature is reduced over time, as well as the specific parameters of the algorithm.

In contrast, quantum annealing (QA) is a quantum computation method used to find the ground state of a system's energy; see Fig. (1)(c). QA operates by evolving the system from an initial Hamiltonian, which is usually simple and convex, to the target Hamiltonian that encodes the optimization problem. This evolution relies on the principles of quantum mechanics, specifically quantum tunneling, to explore the energy landscape. Quan-

tum annealing utilizes quantum fluctuations to escape local minima and tunnel through energy barriers, potentially leading to faster convergence to the global minimum. This approach can be advantageous in navigating complex landscapes with high barriers between local minima. In Fig. (1)(c), the varying energy landscape is shown as the annealing from the initial convex Hamiltonian to the target Hamiltonian taking place in time. The system starts at the ground state of the initial Hamiltonian and remains in the ground state if annealing is sufficiently slow. The blue line shows the state of the system at each moment.

## CIRCULANT GRAPHS IN PHYSICAL SYSTEMS

An all-optical scalable ONN was recently proposed for cyclic graphs; spatial light modulators (SLMs) are used to discretize the optical field where each pixel defines a different pulse amplitude [27]. The SLM with  $M_x \times M_y$  pixels is set up with a transmission function  $\tilde{J}_k$  which multiplies the Fourier transform of the amplitudes at each round trip. The SLM couples the fields with coupling matrix  $J_{ij} \equiv \tilde{J}_{j-i+1}$ , which corresponds to a circulant graph. An alternative setup allows for any general coupling matrix. However, there is an  $N = M_x$  limit to the number of pulses. Circulant graphs such as Möbius ladders therefore lend themselves well to optical solvers, where  $N = M_x \times M_y \sim 10^6$  spins can be defined.

The couplings are often geometrical in polariton condensates, photon condensates, and laser cavities (e.g. the sign and amplitude of the coupling strength depend on the distance between condensates and outflow wavenumber [25]). The condensates arranged in a circle interact with the nearest neighbours, but the interactions beyond this decay exponentially fast. Previously, various ways of establishing long-range interactions in polariton-based XY-Ising machines were discussed. An easier way to achieve the couplings between remote sites is to use digital micro-mirror devices (DMDs) to direct the light across the ring. DMDs were shown to perform complex (amplitude and phase) modulation. By splitting the complex field into real and imaginary parts and using the

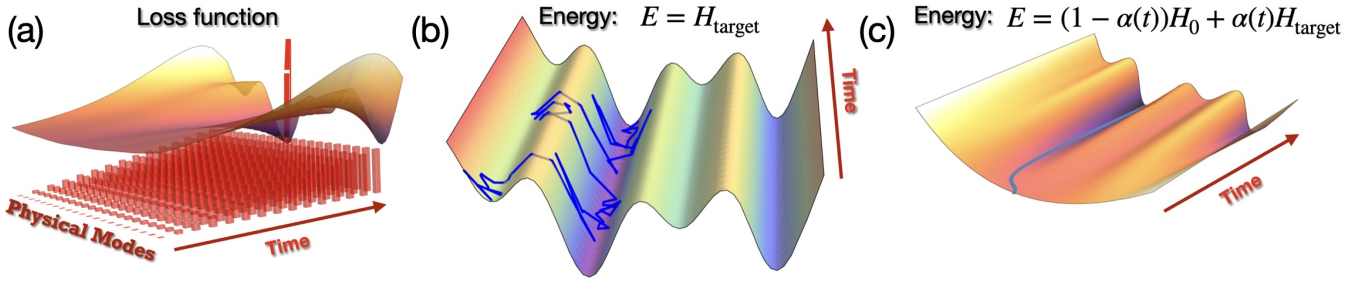


Figure 1. Schematics of the operation of gain-based systems (a), simulated annealing (b), and quantum annealing (c).

time modulation scheme of the DMD, a complex signal could be synthesised [34]. Reflecting the entire ring of condensates on itself with a radial displacement implements a 3-regular cyclic graph. Cyclic graphs are known to be computationally intractable for classical computers for sampling probability distributions of quantum walks [35].

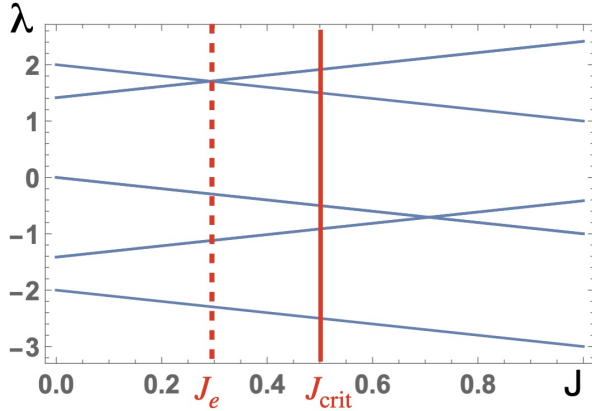


Figure 2. Eigenvalues of the Möbius ladder graph for  $N = 8$  as functions of  $J$ .  $J_e$  is the value of  $J$  where the red dashed line shows the two largest eigenvalues cross.  $J_{\text{crit}}$  shows where their energies equal  $E_1 = E_0$ . The ground state corresponds to  $S_0$  for  $J < J_{\text{crit}}$  and  $S_1$  for  $J > J_{\text{crit}}$ .

### EIGENVECTORS AND EIGENVALUES OF THE MÖBIUS LADDER COUPLING MATRIX

To find the eigenvalues and eigenvectors of  $N \times N$  matrix  $\mathbf{J}$ , for even  $n$  we use the roots of unity, so the solutions of  $\omega^N = 1$  that are  $\omega_k = \exp(i2\pi k/N)$  for  $k = 0, \dots, N-1$ . The corresponding eigenvectors are  $(1, \omega_k, \omega_k^2, \dots, \omega_k^{N-1})$  which can be verified by direct computation. Then, from the first row of  $\mathbf{J}$  we form the polynomial  $f(\omega) = -\omega - J\omega^{N/2} - \omega^{N-1}$  and evaluate it at the unit roots  $\omega_k = \exp[i2\pi k/N]$  to obtain the eigenvalues  $\lambda_k = f(\omega_k) = -2\cos(2\pi k/N) - J(-1)^k$  with the corresponding eigenvectors  $v_k =$

$(1, \omega_k, \omega_k^2, \dots, \omega_k^{N-1})$ . The largest of  $f(\omega_k)$  is either  $\lambda_{N/2} = 2 - J$  or  $\lambda_{N/2\pm 1} = J + 2\cos(2\pi/N)$  depending on whether  $J < J_e$  or  $J > J_e$  with  $J_e \equiv 1 - \cos(2\pi/N)$  is the value where these two eigenvalues cross. The corresponding real-valued, and mutually orthogonal eigenvectors  $\mu_k$  can be formed from  $v(\omega_k)$  as  $\mu_k = \text{Re}[v(\omega_k)] + \text{Im}[v(\omega_k)]$  [32]. For two largest eigenvalues the eigenvectors are  $\mu_{N/2} = (1, -1, 1, -1, \dots, -1)$  and  $\mu_{N/2\pm 1} = (1, \pm \cos(2\pi/N) \pm \sin(2\pi/N), \dots, \pm \cos(2\pi k/N) \pm \sin(2\pi k/N), \dots, \pm \cos(2\pi(N-1)/N) \pm \sin(2\pi(N-1)/N))$ . If  $N/2$  is even, then  $\mu_{N/2\pm 1}$  have the components with two zero values at the positions separated by  $N/2 - 1$  sign alternating components.

We illustrate this construction for the Möbius ladder coupling matrix  $\mathbf{J}$  with  $N = 8$  considered in the main text

$$\mathbf{J} = \begin{pmatrix} 0 & -1 & 0 & 0 & -J & 0 & 0 & -1 \\ -1 & 0 & -1 & 0 & 0 & -J & 0 & 0 \\ 0 & -1 & 0 & -1 & 0 & 0 & -J & 0 \\ 0 & 0 & -1 & 0 & -1 & 0 & 0 & -J \\ -J & 0 & 0 & -1 & 0 & -1 & 0 & 0 \\ 0 & -J & 0 & 0 & -1 & 0 & -1 & 0 \\ 0 & 0 & -J & 0 & 0 & -1 & 0 & -1 \\ -1 & 0 & 0 & -J & 0 & 0 & -1 & 0 \end{pmatrix}. \quad (1)$$

The eigenvalues are  $\lambda_0 = f(\omega_0) = f(1) = -2 - J$ ,  $\lambda_1 = f(\omega_1) = -\sqrt{2} + J$ ,  $\lambda_2 = f(\omega_2) = -J$ ,  $\lambda_3 = f(\omega_3) = \sqrt{2} + J$ ,  $\lambda_4 = f(\omega_4) = 2 - J$ ,  $\lambda_5 = f(\omega_5) = \sqrt{2} + J$ ,  $\lambda_6 = f(\omega_6) = -J$ , and  $\lambda_7 = f(\omega_7) = -\sqrt{2} + J$ .

The eigenvector that corresponds to  $\lambda_3$  is  $\mu_3 = (1, -1, 1, -1, 1, -1, 1, -1)$  and the eigenvector that corresponds to, say,  $\lambda_4$  is  $\mu_4 = (1, -\sqrt{2}, 1, 0, -1, \sqrt{2}, -1, 0)$ . The soft spin system, therefore, follows  $(+, -, +, +, -, +, -, -)$  or  $(+, -, +, -, -, +, -, +)$  direction at the onset of the pitchfork bifurcation when  $J > J_e$  while  $\lambda_4$  becomes the dominant eigenvalue of matrix  $\mathbf{J}$ . Figure 2 illustrates how these eigenvalues vary as a function of  $J$ .

### BASINS OF ATTRACTION

Figure 3 depicts the basins of attraction for various  $p$  and fixed  $J_e < J < J_{\text{crit}}$ . The basins of attraction are defined as the sets of points randomly distributed on  $[-1, 1]$

from which the gradient descent leads to different minima. At the threshold of large negative  $p$ , the basin of attraction of  $E_1$  (which is the ground state of  $E$  as given by Eq. (1) of main text) dominates. As  $p$  increases, the basin of attraction of the excited state  $E_0$  increases while at small positive values of  $p$ ,  $E_0$  becomes the ground state. With a further increase of  $p$  other states with even higher energy appear.

### CRITICAL POINTS

The main text gives the energy of the CIM  $E$  in Eq. (1). We can determine the critical (minima and the saddle) points by setting  $\partial E/\partial x_i = 0$  for all  $i = 1, \dots, N$  and classify them using the Hessian matrix. The number of critical points grows exponentially fast with  $p$ ; however, not in terms of energy and the distance from the state  $x_i = 0 \forall i$  as Fig. 4 illustrates.

### QUANTUM ISING MODEL

We consider the transverse field Ising model with the circulant coupling matrix  $\mathbf{J}$  given by

$$\hat{H} = -\frac{1}{2} \sum_{\substack{i,j=1 \\ i \neq j}}^{N,N} J_{ij} \hat{S}_i^z \hat{S}_j^z - \sum_{i=1}^N h_i \hat{S}_i^z - \gamma(t) \sum_{i=1}^N \hat{S}_i^x, \quad (2)$$

$$\hat{S}_i^\alpha = \mathbf{1} \otimes \mathbf{1} \otimes \dots \otimes \mathbf{1} \otimes \hat{S}^\alpha \otimes \underbrace{\mathbf{1} \otimes \dots \otimes \mathbf{1}}_{i-1 \text{ terms}} \otimes \mathbf{1}, \quad \alpha = x, y, z, \quad (3)$$

where  $\hat{S}^\alpha$  are the spin-1/2 Pauli matrices, and  $\mathbf{1}$  is the  $2 \times 2$  identity matrix. The first term,  $\hat{H}_0$ , is diagonal. The symmetry-breaking longitudinal magnetic field is denoted by  $\hat{H}_1$ . The transverse field,  $\hat{H}_2$ , results in a non-diagonal Hamiltonian operator and gives rise to the quantum Ising model.

Our quantum system is made up of  $N$  spin-1/2 subsystems each having a basis  $|\downarrow\rangle, |\uparrow\rangle$ . A general state  $|\Psi\rangle$  of the  $N$ -spin system can then be written as  $|\Psi\rangle = \sum_{\xi} C_{\xi} |\xi\rangle$  with  $\sum_{\xi} |C_{\xi}|^2 = 1$ , where the  $C_{\xi}$ 's are complex numbers and the basis element  $|\xi\rangle \equiv |\xi_1 \dots \xi_N\rangle = |\xi_N\rangle \otimes \dots \otimes |\xi_1\rangle$ ,  $\xi_k = \{|\downarrow\rangle, |\uparrow\rangle\}$ ,  $k = 1, \dots, N$ .

### SOLUTION OF THE TIME-DEPENDENT SCHRÖDINGER EQUATION

The wavefunction is evolved according to the time-dependent Schrödinger equation (with  $\hbar = 1$ ) given by

$$i \frac{d}{dt} |\Psi(t)\rangle = \hat{H}(t) |\Psi(t)\rangle, \quad (4)$$

$$\hat{H}(t_i) |\Psi(t_i)\rangle = \epsilon_{gs} |\Psi(t_i)\rangle, \quad (5)$$

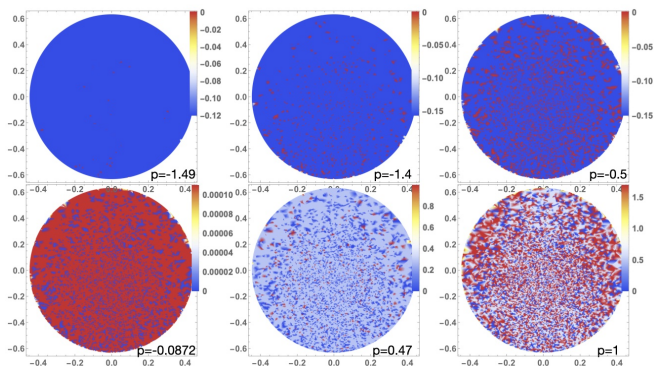


Figure 3. Basins of attraction of the soft spin energy in Eq. (2) as defined in the main text. We take  $N = 8$ ,  $J = 0.4$ ,  $C = 1$ , various laser powers  $p$ , 20,000 randomly distributed  $x_i$  in  $[-1, 1]$  and show which minimum is reached via gradient descent using Newton's method. To characterize points, the average magnetization  $m = \sum_i x_i/N$  (vertical axis) and the correlations along the circle between  $x_i$  defined as  $X_{\text{corr}} = \sum_i (x_i - m)(x_{i+1} - m) / \sum_i (x_i - m)^2$  (horizontal axis), are used. For small  $p$ , the basin of attraction is dominated by  $S_1$  state as any initial state descends to  $E_1$ . As  $p$  grows, the ratio of the volume of the basins of attraction of the  $S_1$  state to the volume of the basins of attraction of the  $S_0$  approaches 4. At the critical value of  $p \approx -0.08715$ , both  $S_1$  and  $S_0$  states have the same energy, and after that  $S_0$  state becomes the ground state: this is indicated by the switch between ground (blue) and excited (red) states.

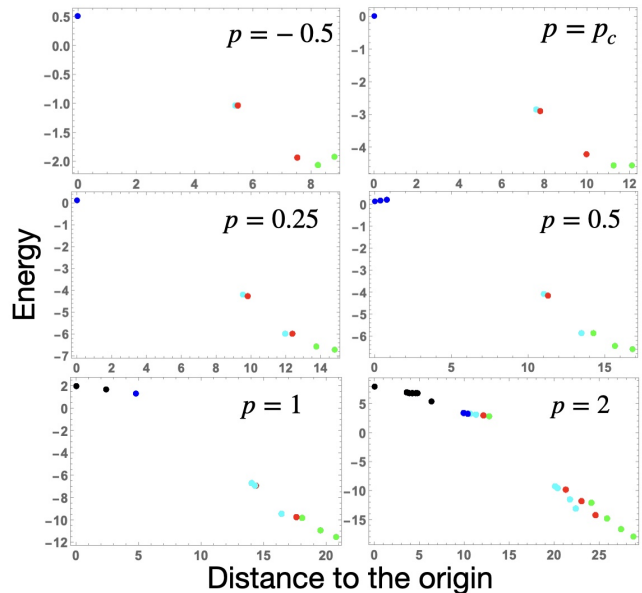


Figure 4. Critical points of the CIM energy (defined by Eq. (1) of the main text) for  $N = 8, C = 1$  and different values of laser power  $p$ . Minima are shown in green, saddles with one, two, three and 4+ unstable directions are shown as red, light blue, blue and black points, respectively. The  $S_0$  state is furthest from the origin, which becomes the global minimum for  $p > p_c = -0.0872$ . The minima for  $p = 2$  are  $S_0, S_1, (-, -, +, -, +, -, -, +), (+, -, -, +, +, -, +, -)$  and  $(+, -, -, +, +, -, -, +)$  in increasing energy.

where  $\epsilon_{gs}$  denotes the ground state energy of the system at the initial time.

To evolve the time-dependent Hamiltonian given by Eq.(4), we use a second order accurate Strang time-splitting method where  $\hat{H}_0$  is evolved for half a time-step  $\Delta t$  followed by  $\hat{H}_1$  for a full time-step and then  $\hat{H}_0$  for another half a time-step. The resulting time-integration scheme can then be written as

$$|\Psi(t_{n+1})\rangle = \exp\left(-i\frac{\Delta t}{2}\hat{H}_D\right)\left(-\frac{i}{2}\int_{t_n}^{t_{n+1}}\hat{H}_2(\tilde{t})d\tilde{t}\right) \times \exp\left(-i\frac{\Delta t}{2}\hat{H}_D\right)|\Psi(t_n)\rangle, \quad (6)$$

where  $\hat{H}_D = \hat{H}_0 + \hat{H}_1$  is the diagonal part of the Hamiltonian operator.

By placing the Hamiltonian operator  $\hat{H}_2(t)$  containing the time-dependent term in the middle of the split-step algorithm, we ensure that we have a symmetric time-splitting method. The time integral appearing in Eq. (6) was evaluated analytically. In our simulations, we set  $\Delta t \equiv t_{n+1} - t_n = 0.1$ . The simulations were performed in MATLAB. The exponentials of the diagonal and non-diagonal Hamiltonian can then be readily evaluated using the `expm` function [44].

## COMPUTATION OF BLOCH VECTORS IN QUANTUM ANNEALING SIMULATIONS

The single-spin reduced density matrix  $\hat{\rho}_{1,k}$  is obtained by taking the partial trace of the  $2^N \times 2^N$  density matrix  $\hat{\rho}$  over the Hilbert space of the other  $N-1$  spins. For the  $k$ 'th spin, this is defined as

$$\hat{\rho}_{1,k}(t) = \text{Tr}_{\{N \setminus k\}} \hat{\rho}, \quad (7)$$

where  $\{N \setminus k\}$  denotes the  $N$  spin Hilbert space excluding the  $k$ 'th spin. The single-spin density matrix can then be parameterised as

$$\hat{\rho}_{1,k} = \frac{1}{2} (\mathbf{1} + \mathbf{u}_k \cdot \hat{\mathbf{S}}) = \frac{1}{2} \begin{pmatrix} 1 + w_k & u_k - iv_k \\ u_k + iv_k & 1 - w_k \end{pmatrix}, \quad (8)$$

where  $\mathbf{u}_k = (u_k, v_k, w_k)$  defines the corresponding Bloch vector and  $\hat{\mathbf{S}} = (\hat{S}^x, \hat{S}^y, \hat{S}^z)$  correspond to the vector of spin-1/2 Pauli matrices. For pure states the single-spin reduced density matrix has rank 1, with a magnitude of the Bloch vector  $|\mathbf{u}_k| = 1$ . The surface of the Bloch sphere, therefore, represents all the possible pure states whereas the interior of the sphere corresponds to mixed states. The collapse of the Bloch vector towards the origin implies that the state represents a maximally entangled Bell-like state.

## MASTER EQUATION FOR CLASSICAL/SIMULATED ANNEALING

To model simulated annealing, we follow the method described in [43] and introduce the Master equation for the transition probability  $P_i(t)$  for each spin configuration.

$$\frac{dP_i(t)}{dt} = \sum_{j=1}^{2^N} A_{ij}(t)P_j(t) \quad (9)$$

The  $2^N \times 2^N$  matrix  $A_{ij}(t)$  describes the transition rates. The master equation can be written in the form

$$\frac{dP_i(t)}{dt} = \sum_{i \neq j} A_{ij}(t)P_j(t) + A_{ii}(t)P_i(t) \quad (10)$$

$$= \sum_{i \neq j} (A_{ij}(t)P_j(t) - A_{ji}(t)P_i(t)) \quad (11)$$

where we have made use of the conservation of probability given by

$$\frac{d}{dt} \sum_j P_j(t) = \sum_{i,j} (A_{ji}P_i) = 0, \quad (12)$$

to arrive at the final equality. Since the normalisation condition must hold for any probabilities  $P_j$ , it follows that

$$\sum_j A_{ji} = 0, \quad \text{or} \quad A_{ii} = -\sum_{i \neq j} A_{ji}. \quad (13)$$

Using Eq.(13) to represent the diagonal terms of the Master equation ensures that a numerical integration of this equation continues to conserve the normalisation of the probabilities.

The precise form of the transition probabilities is problem specific although it is common to use the Boltzmann distribution. In our work, we follow [43] and use the Bose-Einstein distribution such that

$$A_{ij}(t) = \begin{cases} \left\{ 1 + \exp\left[\frac{(E_i - E_j)}{T(t)}\right] \right\}^{-1}, & (\text{single-spin flip}) \\ -\sum_{k \neq i} A_{ki}, & (i = j) \\ 0, & (\text{otherwise}). \end{cases}$$

The form given above that is used for our simulated annealing simulations means that entries of  $A_{ij}$  are non-zero only for transitions corresponding to single-spin flips. The annealing is performed by varying the temperature  $T(t)$  with time. To maintain consistency with our quantum annealing simulations, we have varied the temperature according to  $T(t) = D/\sqrt{t}$ , where  $D$  is a free parameter which we set to  $D = 5$ .

For our classical annealing (CA) simulations, we did not zero out any of the transition probabilities in order to infer how collective transitions of spins at each time-step,

that are associated with spin correlations, as opposed to only single-spin transitions, affects the performance of classical algorithms. Such collective transitions can be important when frustration arises with particular spin configurations that can render certain single-spin transitions ineffective at escaping local energy minima. It is also useful to make the observation that quantum and classical annealing can be closely related to one another if one formulates quantum annealing in imaginary time following a Wick rotation. It then follows that the evolution of the  $N$ -spin wavefunction  $|\Psi(t)\rangle$  is given by

$$\frac{d}{dt}|\Psi(t)\rangle = (\mu(t) - \hat{H}(t))|\Psi(t)\rangle. \quad (14)$$

Here,  $\mu(t)$  plays the role of a Lagrange multiplier which ensures that the normalisation of the wavefunction is conserved in analogy with the modification introduced above to the diagonal term of the Master equation. Therefore, by comparing quantum annealing, simulated annealing, and classical annealing, we can distinguish between the effects of retaining all-spin transitions from the difference of evolving our equations in real and imaginary time.

## RESULTS OF ANNEALING SIMULATIONS

Here, we include additional simulation results to complement the results presented in the main text. In Figs. 2f and 2g of the main text, we presented results for the time evolution of the ground state probability for  $J = 0.35$  and  $B = 5$ . In Fig. 5, we also present results for  $J = 0$  for the probability amplitude of the eigenstates with the two energy minima to discern the role of ground state degeneracy and how this is lifted by the symmetry breaking terms. In Figs. 5a and 5b we present simulations for the case where no symmetry breaking term is included so that the system contains two degenerate energy minima. Time evolution of the probabilities for finding the system in one of the two degenerate ground states show an equal probability for the system to be found in either one of these states. Moreover, the results are relatively similar regardless of which numerical method is considered. Therefore, all models including QA, SA and CA show a similar performance in tracking the ground states as indicated by the curves representing adiabatic evolution of the system.

In Figs. 5c and 5d we present simulations for the case where a symmetry breaking term is included as in the main text. Here, we used  $0.05|\xi\rangle_{S_0} + 0.05|\xi\rangle_{S_1}$  to introduce the symmetry breaking term. In contrast to the previous case, the behaviour of the different models is now markedly different. In particular, we observe that both QA and CA correctly evolve with the true ground state as indicated by the curves corresponding to the adiabatic evolution. Moreover, due to the symmetry breaking there is one unique ground state that the two meth-

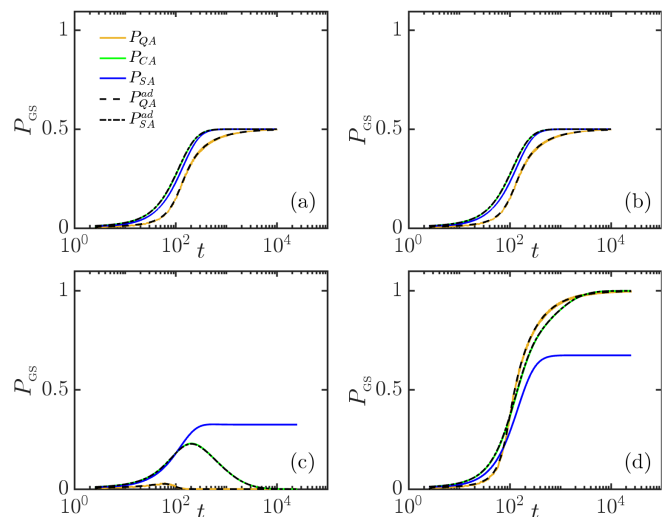


Figure 5. Time-evolution of ground state probability of target Hamiltonian with  $J = 0$  and  $B = 5$  for quantum annealing (QA), single-spin simulated annealing (SA), classical annealing (CA) and corresponding probabilities expected for adiabatic simulated (SA-ad) and adiabatic quantum (QA-ad) annealing. (a) and (b) correspond to simulation without symmetry breaking term which corresponds to a doubly degenerate ground state. Each figure corresponds to the projection of the probability density onto each one of the ground states; (c) and (d) correspond to a simulation with a symmetry breaking term added which lifts the degeneracy and leads to a unique ground state.

ods can follow. In contrast, simulated annealing is not always successful at tracking the true ground state even for this case where  $J = 0$ . We found a success probability of only 67%, whereas the remaining probability is associated with the system converging to what is now a metastable state.

Given the close analogy between CA and QA identified at the end of the previous section, it is interesting to observe that both methods perform well in the test case presented in Fig. 5 whilst SA fails. This points to the important role played by inter-spin correlations that are encoded in the transition matrix that is absent in SA. Nevertheless, it is known that provided a sufficiently slow annealing schedule is used, SA will still converge to the correct ground state although the long annealing times involved make this approach impractical for solving hard optimization problems. To demonstrate this, we have performed additional simulations for the case of  $J = 0$  with a symmetry breaking term as before and with two different annealing schedules corresponding to  $\gamma(t) = T(t) = B/\ln(t + t_0)$  and  $B/\sqrt{t + t_0}$ , where  $t_0 = 0.5$ . Results presented in Fig. 6 show that for the former, even SA appears to asymptote to the correct ground state but the convergence is remarkably slow. Reducing the value of  $B$  appears to deteriorate the success probability of finding the ground state for SA. For the second schedule

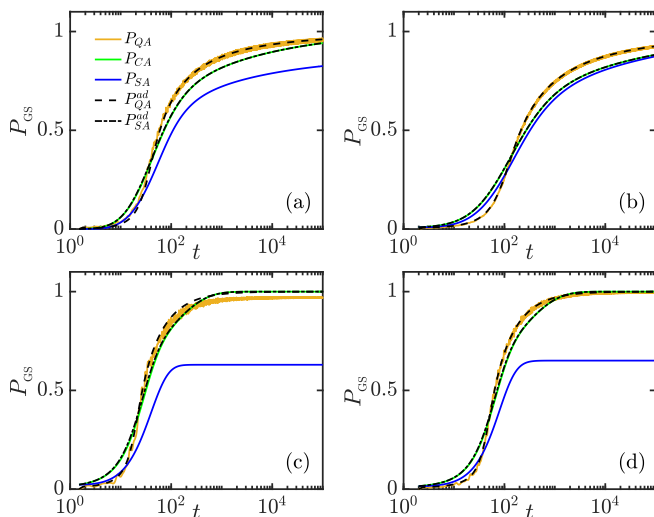


Figure 6. Time-evolution of ground state probability of target Hamiltonian with  $J = 0$  with a symmetry breaking term of the form  $0.05|\xi\rangle_{S_0} + 0.05|\xi\rangle_{S_1}$  added for quantum annealing (QA), single-spin simulated annealing (SA), classical annealing (CA) and corresponding probabilities expected for adiabatic simulated (SA-ad) and adiabatic quantum (QA-ad) annealing. (a) and (b) correspond to simulation with  $B = 3$  and  $B = 4$ , respectively with annealing schedule  $\gamma(t) = T(t) = B/\ln(t + t_0)$ ; (c) and (d) correspond to simulation with  $B = 3$  and  $B = 4$ , respectively with annealing schedule  $\gamma(t) = T(t) = B/\sqrt{t + t_0}$ .

we tested, SA appears to always fail for the range of  $B$  values tested. In contrast, QA and CA continue to perform better and demonstrate the advantage of the two methods that we attribute to the role played by interspin correlations.

In order to perform a more systematic study of the impact of including the symmetry breaking terms on QA, in Fig. 7 we present results of simulations obtained with a symmetry breaking term of the form  $0.05|\xi\rangle_{S_0} + h_1|\xi\rangle_{S_1}$ , where  $h_1$  is varied from 0.005 to 0.1. For each value of  $h_1$ , we have evaluated the time evolution of the probability amplitudes  $\langle \uparrow | \hat{\rho}_{1,k} | \uparrow \rangle$  for each spin  $k$  as well as the time evolution of the magnitude of the corresponding Bloch vectors  $|\mathbf{u}_k|$ . The results demonstrate that as  $h_1$  is increased, the initial evolution of the probability amplitudes is to align the spins towards the  $S_1$  state which is caused by the increasing contribution of the symmetry breaking term. However, as the system navigates the energy landscape, quantum correlations develop as indicated by the decreasing amplitude of the Bloch vectors of the individual spins. This emerging quantum entanglement of the spins prevents the system from becoming stuck in local energy minima and subsequently allows the spins to readjust in order to track the true ground state. Subsequently the system converges to the true ground state that is well described by a pure state as the magnitude of the Bloch vectors converge to unity. We note that during the evolution, the maximal entanglement oc-

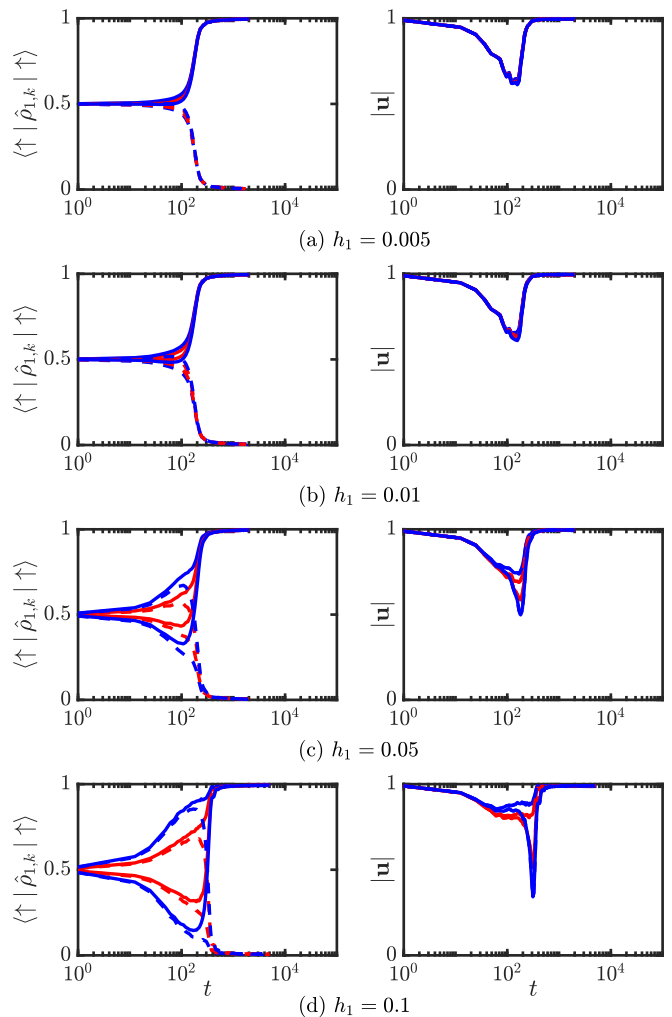


Figure 7. Time-evolution of probability amplitude of  $|\uparrow\rangle$  state (left panels) and magnitude of Bloch vectors (right panels) in quantum annealing computation with  $J = 0.35$  and  $B = 5$ . The dashed lines correspond to spins that at the end of the annealing align along the  $|\downarrow\rangle$  state whereas solid lines correspond to spins that align with the  $|\uparrow\rangle$  state. The red and blue colored lines correspond to the color of the spins shown in Fig. 1b of main text.

curr at the time when the projection of some of the spins flips to the opposite direction. This time also coincides with the time where SA fails to track the correct ground state in comparison to QA as reflected in the results of Figs. 5c and 5d. We, therefore, conclude that quantum correlations play a key role in allowing QA to outperform other methods in this region of the parameter space of the Möbius circulant graph.

\* correspondence address: [N.G.Berloff@damtp.cam.ac.uk](mailto:N.G.Berloff@damtp.cam.ac.uk)